Supporting Information

Bioinspired value-added conversion of rotten bread into porous vanadium oxide-vanadium carbide@carbon composites for high-rate Zn- and Li-ion batteries

Sateesh Panugamti,[a] Bhargav Akkinepally,[a]* Samikannu Prabu,[b] Chandra Sekhar Sale,[d] Nagaraju Goli,[c]*Jaesool Shim[a]*

[a]*School of Mechanical Engineering, Yeungnam University, Gyeongsan 38541, Republic of Korea*

[b]*School of Chemical, Biological and Battery Engineering, Gachon University, 13120 Seongnam, Republic of Korea*

[c]*Department of Materials, Imperial College London, South Kensington Campus, London-SW7 2AZ, United Kingdom*

[d]*School of Chemical, Materials, and Biological Engineering, The University of Sheffield, Sheffield S1 3JD, United Kingdom*

Correspond authors:

bhargav@ynu.ac.kr (B.A.)

nagarajugoli7@gmail.com (N.G)

jshim@ynu.ac.kr (J.Shim)

Formation process of VO-VC composite: During the thermal treatment, vanadium precursor ($VOSO_4 \cdot xH_2O$) undergoes dehydration and decomposition, followed by conversion to vanadium oxide under an inert atmosphere in the presence of the carbon matrix. The overall transformation can be described in a simplified form as follows:

Step 1: Dehydration:

$$VOSO_4 \cdot xH_2O \rightarrow VOSO_4 + xH_2O\uparrow$$

Step 2: Thermal decomposition under an inert atmosphere:

$$VOSO_4 + C \rightarrow VO_x + SO_2\uparrow + CO_2\uparrow$$

Step 3: Carbothermal reduction (carbon-assisted formation of vanadium oxide and carbide phases):

$$VO_x + C \rightarrow VO + CO\uparrow$$

$$V + C \rightarrow VC$$

Under the carbon-rich and reducing environment generated during pyrolysis, partial reduction of vanadium species leads to mixed VO/VO_2 formation, while simultaneous carbon-vanadium interaction at higher temperature facilitates VC formation, resulting in the VO-VC heterostructure embedded in the carbon matrix.

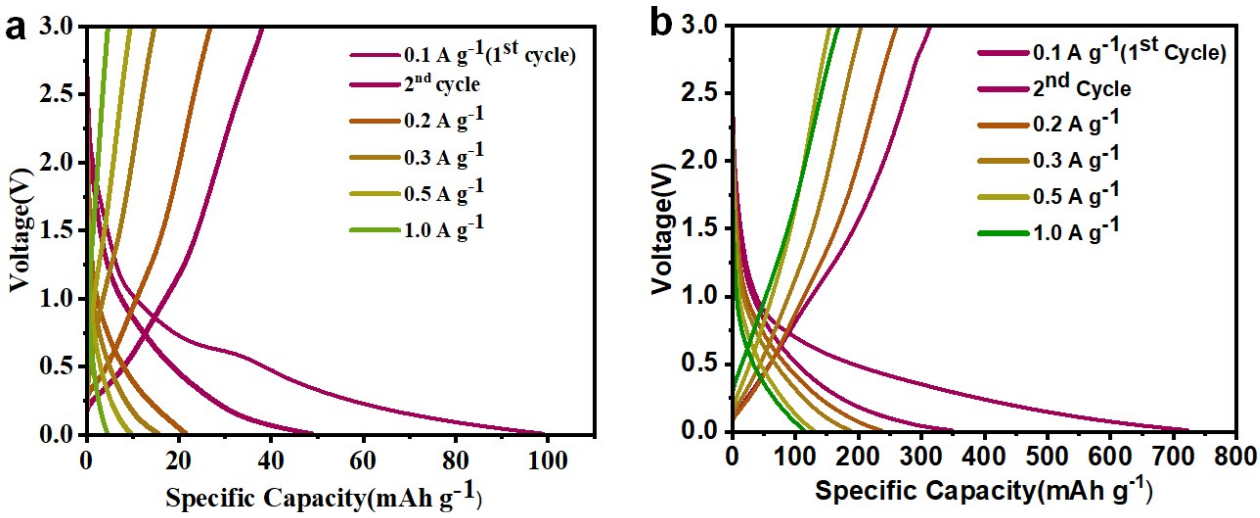

Figure S1. Charge-discharge curves of bare VO and VO-VC@700 electrode at different current densities.

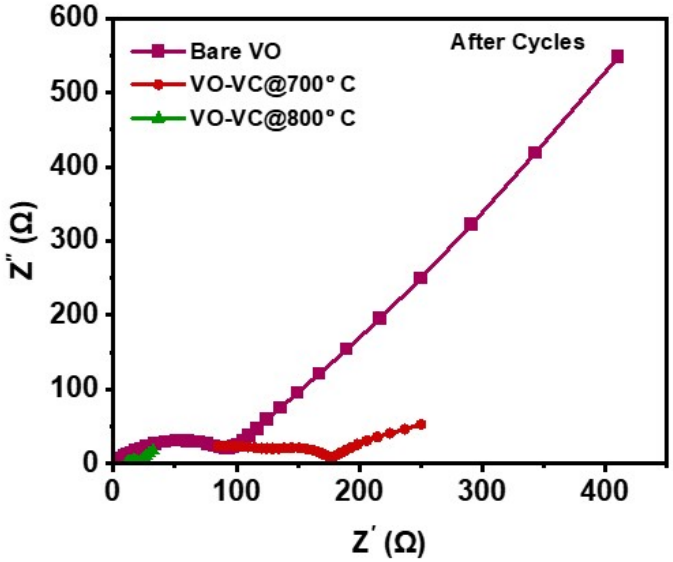

Figure S2. Nyquist plots of the fabricated Li-ion batteries using various electrodes after cycling stability.

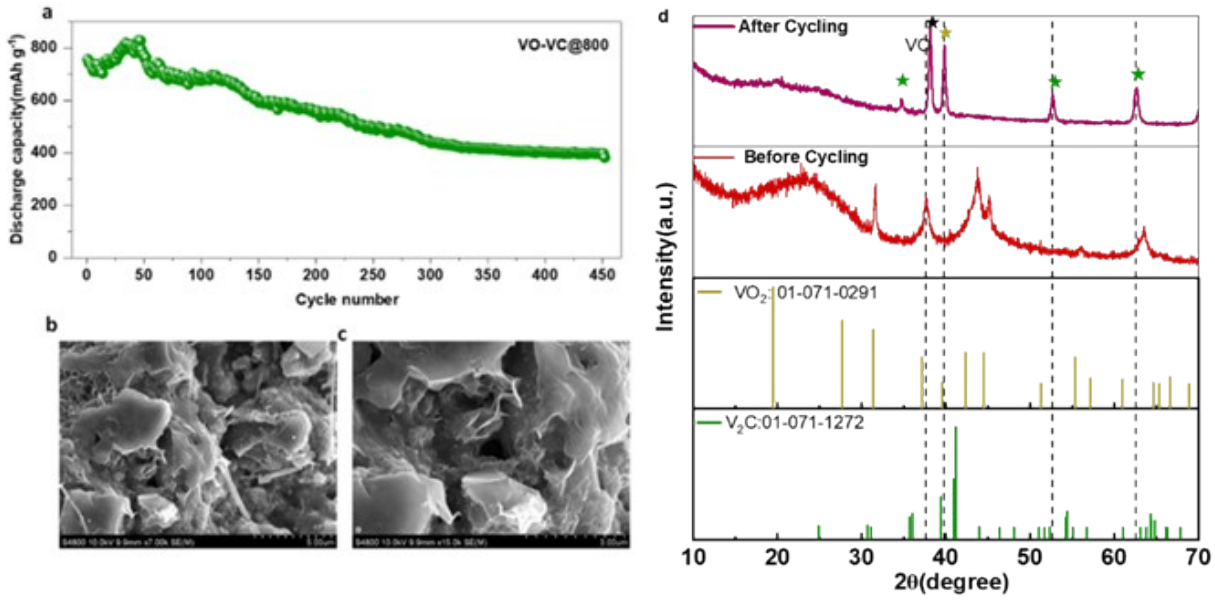

Figure S3. Long-term cycling stability of Li-ion battery cell fabricated with VO-VC@800 electrode and corresponding post-cycling SEM images of the VO-VC@800, and post-cycling XRD analysis of the corresponding electrode.

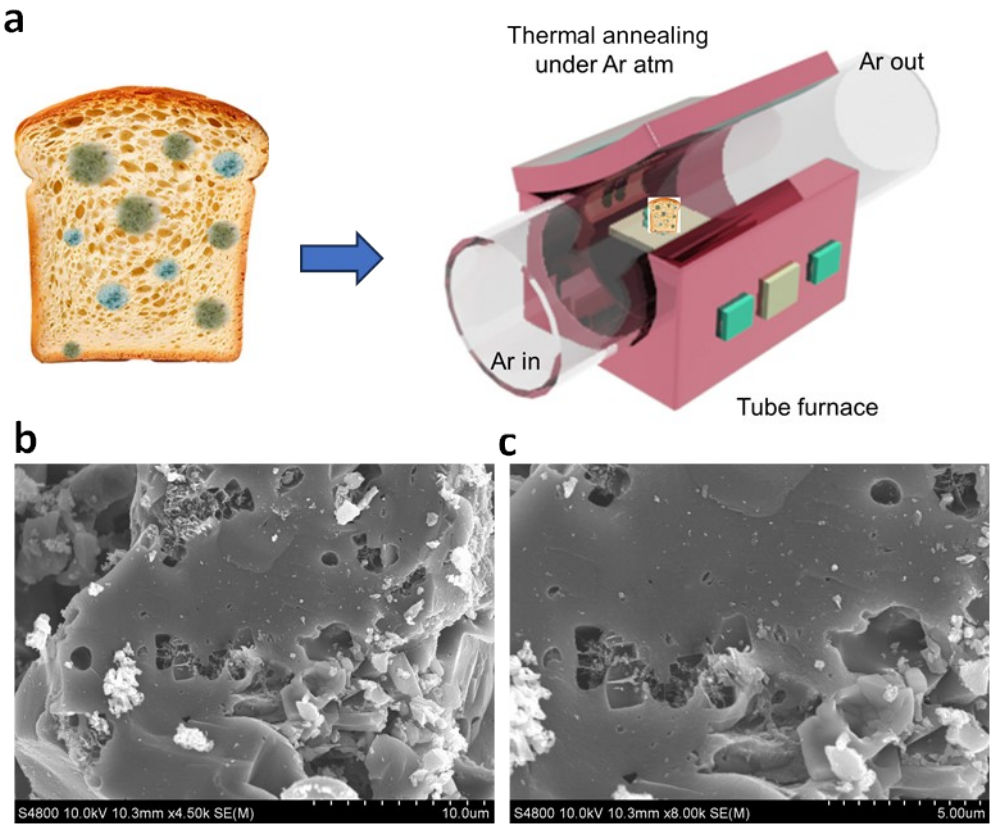

Figure S4. (a) Schematic representation and (b-c) SEM images of the rotten-bread-derived carbon after annealing at 800 °C under Ar gas flow.

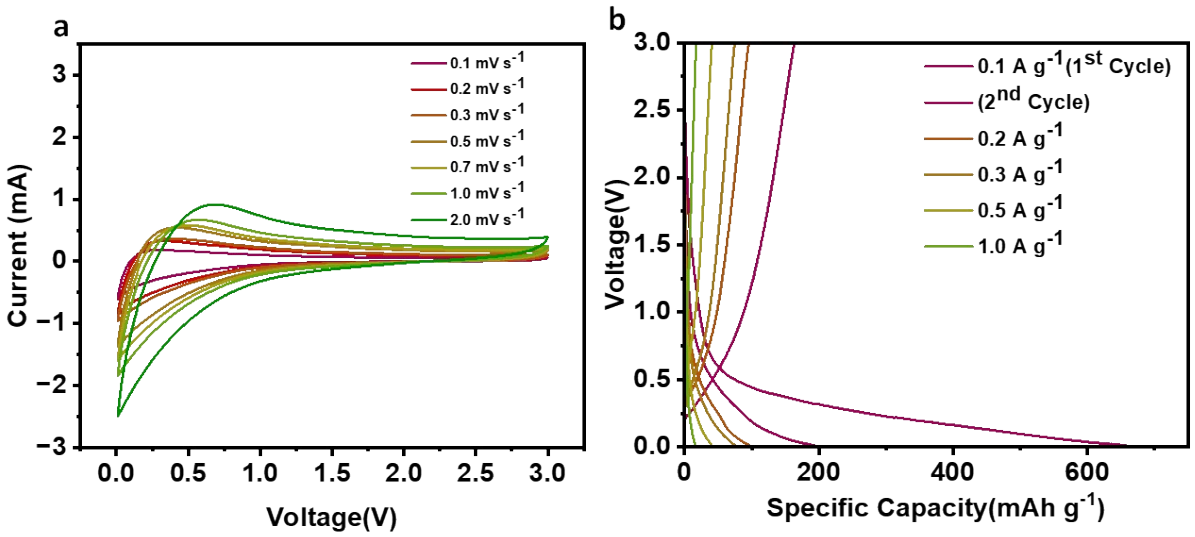

Figure S5. CV and charge-discharge curves of a Li-ion battery fabricated using bread-derived carbon.

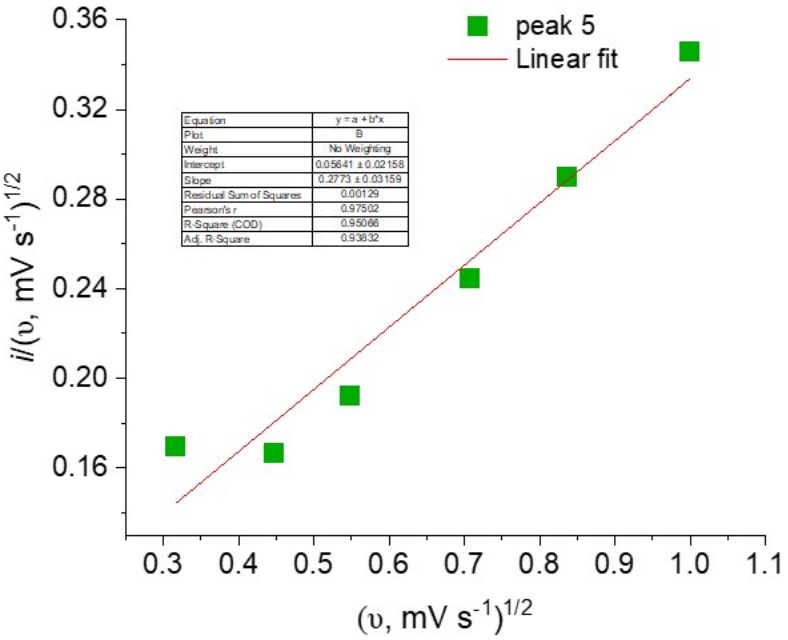

Figure S6. The modified power law derivatives and relationship of $v^{1/2}$ *vs.* $i/v^{1/2}$.

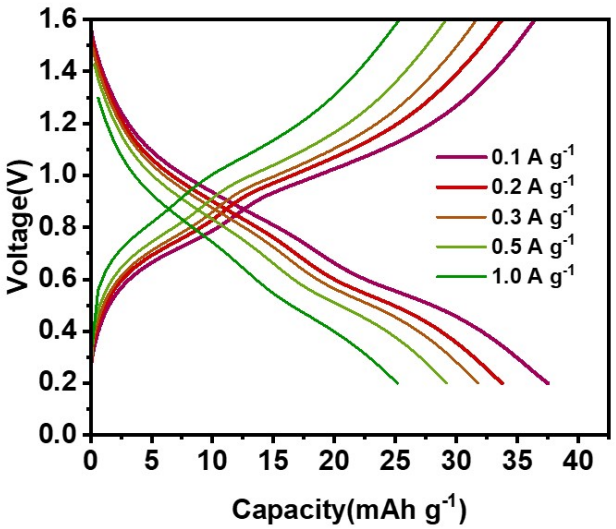

Figure S7. Charge-discharge curves of ZIB with a higher mass loading of the VO-VC@800 electrode.[1,2]

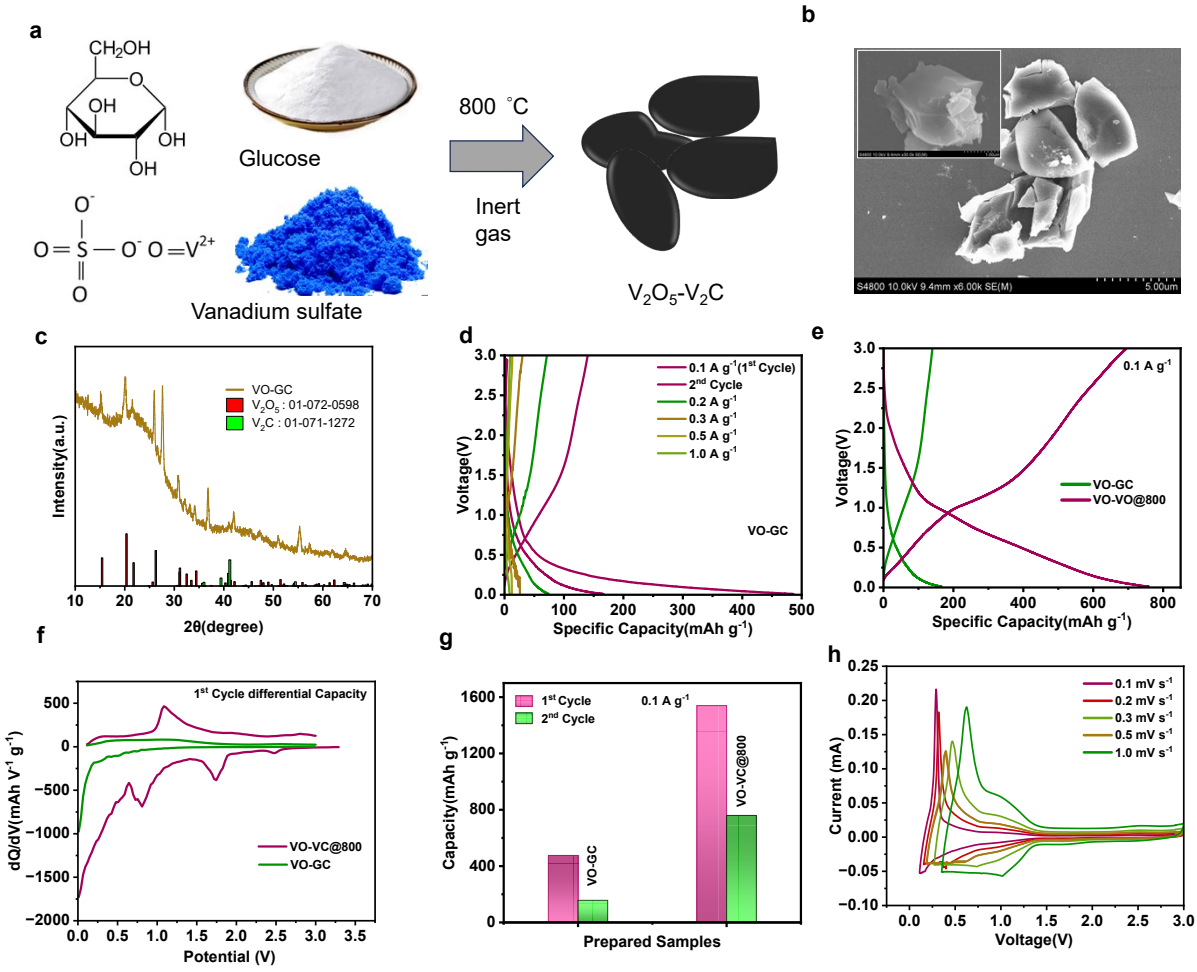

Figure S8. (a) Synthesis process of glucose-assisted synthesis of VO-GC (V_2O_5-V_2C), which was carried out using the similar procedure used for bread-derived VO-VC@800. (b) FE-SEM images of VO-GC], showing the randomly distributed particle shape with dense surface morphology and c) XRD spectrum of VO-GC. Li-ion battery performance of VO-GC as anode in comparison with bread-derived VO-VC@800; d) galvanostatic charge-discharge profiles of VO-GC-based cell at different current densities, e) comparative charge-discharge profiles of VO-GC and VO-VC@800-based cells at a current density of 0.1 A/g. f) Comparative dq/dV profiles and g) capacity plots of VO-GC and VO-VC@800- based Li-ion battery cells. (h) CV curves of the VO-GC at different scan rates of 0.1-1 mV/s.

The structural comparison between bread- and other carbon-precursor based vanadium-carbon sample was also examined. Figure S8a shows the preparation process of glucose-derived V2O5-

V2C carbon sample prepared under similar conditions of VO-VC@800. Figure S8a and S8b shows the FE-SEM images of glucose-derived VO-GC (V_2O_5-V_2C), which shows interconnected layered structures with bulk morphology. Under the magnified condition (inset of Figure S8b), the SEM images show the surface of VO-GC particles showed dense morphology without porous features, as like VO-VC@800 derived from the waste bread-based precursor. The dense architecture of VO-GC could be expected to provide low active surface areas and facilitate poor electrolyte penetration. The XRD pattern of VO-GC in Figure S8c shows more crystalline peaks related to V_2O_5 (JCPDS: 072-0598) and relatively low peaks were noticed for V_2C (071-1272), indicating the heterostructure formation in glucose derived VO-GC is relatively poor. The electrochemical and structural properties of the glucose derived VO-GC electrode were systematically investigated to evaluate its lithium-ion storage performance. This behavior suggests that the heterostructure formation is crucial to provide lower charge transfer resistance for efficient charge transport within the electrode. The charge-discharge profiles in Figure S8d exhibit the VO-GC sample showed lithium-ion insertion/extraction behavior with moderate polarization, confirming the VO-GC material showed the specific capacity of 484.4 mAh/g and 165.3 mAh/g for the 1st and 2nd cycles at a current density of 0.1 A/g. When the current density was increased to 1 A/g, the capacity of VO-GC cell only showed a capacity of 9 mAh/g with a poor rate capability 0.05%. The poor rate capability could be ascribed due to the increased polarization, and it indicates relatively lower charge-storage capability and slower electrochemical kinetics. The comparative capacity plots and dq/dv of VO-GC with VO-VC@800 sample were included in Figure S8e-g, which clearly demonstrate that the VO-VC@800 derived-from the bread outperform the glucose-derived VO-VC and these results confirm the waste- carbon source of bread is crucial in controlling the structural and electrochemical performance. Additionally, the redox behaviour was further validated, as presented in Figure S8h. The CV curves recorded at different scan rates of VO-GC based cells show distinct redox peaks associated with the reversible oxidation/reduction reactions of vanadium species are observed, confirming the pseudocapacitive contribution of the electrode. Nevertheless, the broader peak shape and slight peak shifts suggest comparatively slower electron-transfer kinetics and reduced reversibility than VO-VC@800. Although the glucose-derived carbon matrix provides conductive pathways and electroactive sites, the electrochemical performance remains lower due to insufficient graphitization and reduced conductivity. However, the structural compactness and limited conductive network may restrict rapid ion/electron transport

during cycling. Overall, these results shows that glucose derived VO-GC electrode exhibits Li-ion storage electrochemical activity; however, its performance is comparatively lower than that of bread-derived VO-VC@800. The improved performance of VO-VC@800 can be attributed to enhanced carbon graphitization, improved electrical conductivity, faster ion diffusion, and better structural stability achieved at the optimized carbonization temperature of 800 °C.

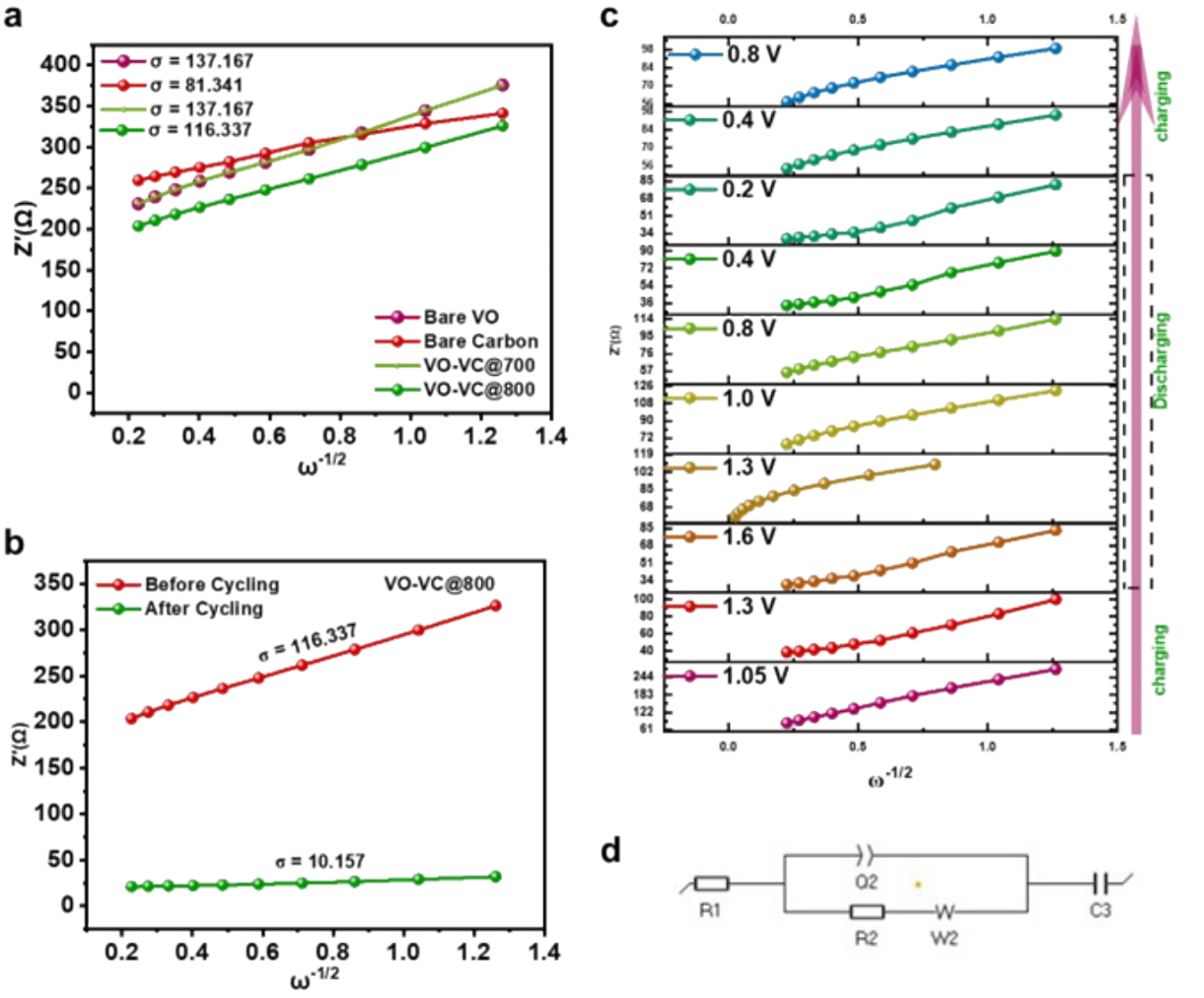

Figure S9. a) Linear fitting plots of $\omega^{-1/2}$ versus Z' in the low frequency regions of Li-ion battery cells using bare VO, bare carbon, VO-VC@700, VO-VC@800. b) Comparison of linear fitting plots of before and after cycling of Li-ion battery cell with VO-VC@800. c) Linear fitting plots of Z' versus $\omega^{-1/2}$ of VO-VC@800 obtained from *in-situ* EIS measurements at different Voltages for the VO-VC@800 ZiB electrode. (d) circuit diagram.

Table S1. Comparative electrochemical performance of vanadium-based materials with our VO-VC@800 materials.

Material	Synthesis	Current density (mA g^{-1})	1st charge Capacity (mAh g^{-1})	Capacity (mAh g^{-1})/ cycle no.	Reference
Li_3VO_4/C	Sol-gel method	100	405	281	3
V2O3/C	Sol-gel thermolysis	100	302	335	4
LVO/C	Ball-milling and calcination method	100	902	561	5
V_2O_3/C	Facile synthesis	100	508	460	6
VO_2/C		50	860	569	7
V_2O_3/C	electrospinning	100	680	570	8
V_2O_3/G	Solid State Synthesis	50	1097	610	9
V_2O_3/C	Solvothermal Synthesis	100	641	386	10
V_2O_3/C	Facile Synthesis	100	1258	856	11
V_2O_3/C	Solvothermal method and Heating Process	100	475	508	12
V_8C_7/RGO	Hydrothermal synthesis /annealing	100	1280	1059	13
V_2O_3/ordered mesoporous carbon)	--	100	857	536	14
VO-VC	Impregnation method	100	1508	759.2	This Work

Electrode Material	Synthesis Method	Diffusion Coefficients(cm^2/s^{-1})	References
VO-VC	Impregnation Method	9.26×10^{-11}	This work
V_2O_5/carbon Nano tubes	Solvothermal	5.44×10^{-12}	15
2D V_2O_5@C NS	Precipitation	6.42×10^{-14}	16
CVO(CoV_2O_6)	Coprecipitation	2.65×10^{-13}	17
V_2O_5/MWCNT	Solvothermal	2.01×10^{-12}	18
V_2O_5@C	---	3.86×10^{-11}	19
Ga-doped V_6O_{13}	Solvothermal Method	3.63×10^{-14}	20
V_2O_5/Carbon Nanotube	----	3.78×10^{-9}	21

Table S2. Comparison of Diffusion Coefficients of Vanadium-based materials with our sample.

Voltage(V)	Sigma Values	Diffusion coefficients ($cm^2\ s^{-1}$)
1.05 (OCV)	183.248	$1.81 \times 10^{?\ 15}$
1.3	59.445	$1.72 \times 10^{?\ 14}$
1.6	52.410	$2.21 \times 10^{?\ 14}$
1.3	63.321	$1.51 \times 10^{?\ 14}$
1.0	52.52	$2.20 \times 10^{?\ 14}$
0.8	54.59	$2.04 \times 10^{?\ 14}$
0.4	56.37	$1.91 \times 10^{?\ 14}$
0.2	39.25	$3.95 \times 10^{?\ 14}$
0.4	39.25	$3.95 \times 10^{?\ 14}$
0.8	39.27	$3.94 \times 10^{?\ 14}$

Table S3. Calculated diffusion coefficients of Zn^{2+} in the zinc ion battery at different Voltages.

References

1 Y. Zhang, Y. Xiao, L. Chen and S. Hu, *J. Mater. Chem. A Mater.*, 2024, **12**, 16537–16545.

2 K. Fu, K. Sun, X. Li, H. Yang, X. He, S. Zhai, L. Gong and P. Tan, *Sustain. Energy Fuels*, 2025, **9**, 1656–1671.

3 (PDF) Sol-gel synthesis of Li3VO4/C composites as anode materials for lithium-ion batteries, https://www.researchgate.net/publication/346554978_Sol-gel_synthesis_of_Li3VO4C_composites_as_anode_materials_for_lithium-ion_batteries, (accessed 27 December 2025).

4 G. S. Zakharova, E. Thauer, A. N. Enyashin, L. F. Deeg, Q. Zhu and R. Klingeler, *Journal of Sol-Gel Science and Technology 2021 98:3*, 2021, **98**, 549–558.

5 S. Li, Z. Qu, S. Luo, Y. Guo, Z. Wan and X. Kong, *ChemElectroChem*, 2020, **7**, 3984–3990.

6 J. H. Kim, Y. S. Kim, S. H. Moon, D. H. Park, M. C. Kim, J. H. Choi, J. H. Shin and K. W. Park, *Electrochim. Acta*, 2021, **389**, 138685.

7 H. E. Wang, X. Zhao, K. Yin, Y. Li, L. Chen, X. Yang, W. Zhang, B. L. Su and G. Cao, *ACS Appl. Mater. Interfaces*, 2017, **9**, 43665–43673.

8 P. Liang, K. Zhu, Y. Rao, H. Zheng, Z. Yao, M. Wu, J. Zhang, J. Liu, K. Yan, J. Wang, Q. Xia and H. Xia, *ACS Appl. Energy Mater.*, 2022, **5**, 3242–3251.

9 S. Petnikota, J. J. Toh, J. Y. Li, R. Chua and M. Srinivasan, *ChemElectroChem*, 2019, **6**, 493–503.

10 C. Huan, X. Zhao, X. Xiao, Y. Lu, S. Qi, Y. Zhan, L. Zhang and G. Xu, *J. Alloys Compd.*, 2019, **776**, 568–574.

11 L. Meng, R. Guo, F. Li, Y. Ma, J. Peng, T. Li, Y. Luo, Y. Li and X. Sun, *Energy Technology*, 2020, **8**, 1900986.

12 J. H. Kim, Y. S. Kim, S. H. Moon, D. H. Park, M. C. Kim, J. H. Choi, J. H. Shin and K. W. Park, *Electrochim. Acta*, 2021, **389**, 138685.

13 J. Yang, L. Li, Y. Zhang, Y. Zhang, C. Sun, H. Tan, W. Huang, Q. Yan and X. Dong, *ChemistrySelect*, 2016, **1**, 2682–2686.

14 L. Zeng, C. Zheng, J. Xi, H. Fei and M. Wei, *Carbon N. Y.*, 2013, **62**, 382–388.

15 X. Liang, G. Gao, S. Feng, Y. Du and G. Wu, *J. Alloys Compd.*, 2019, **772**, 429–437.

16 Wang, X., Jia, W., Wang, L., Huang, Y., Guo, Y., Sun, Y., Jia, D., Pang, W., Guo, Z., Tang, X. *Journal of Materials Chemistry A* , 2016, 4.36: 13907-13915.

17 E. Park, S. So and J. Hur, *Appl. Surf. Sci.*, 2022, **579**, 152182.

18 T. Partheeban, T. Kesavan, M. Vivekanantha and M. Sasidharan, *Appl. Surf. Sci.*, 2019, **493**, 1106–1114.

19 Y. Zhang, A. Pan, Y. Wang, W. Wei, Y. Su, J. Hu, G. Cao and S. Liang, *ACS Appl. Mater. Interfaces*, 2016, **8**, 17303–17311.

20 X. Wu, Z. Zou, S. Li and Y. Zhang, *Ionics 2019 25:10*, 2019, **25**, 4557–4565.

21 Z. Tong, J. Hao, K. Zhang, J. Zhao, B. L. Su and Y. Li, *J. Mater. Chem. C Mater.*, 2014, **2**, 3651–3658.